DOI: 10.24352/UB.OVGU-2019-008 TECHNISCHE MECHANIK, 39, 1, (2019), 72 – 84
submitted: July 6, 2018

Heat Transfer across the Free Surface of a Thermocapillary Liquid Bridge

F. Romanò[1], H. C. Kuhlmann[2]

The heat transfer across the free surface of a millimetric thermocapillary liquid bridge is investigated for two dimensional axisymmetric flows, computed by Newton–Raphson iteration. The coupled multiphase flow in the silicone-oil liquid bridge and in the ambient gas (air) is considered for Marangoni and Prandtl numbers of interest for typical space experiments. Based on the space-resolved heat flux of the two-phase flow for a wide range of parameters, we derive a model for the heat flux in form of Newton's heat transfer law for a surrogate single phase flow, in which a space-dependent Biot function is considered. A parametric study for a 2 cSt silicone-oil liquid bridge is conducted for 150 configurations to derive a reliable fit of the Biot function for a wide range of Reynolds numbers and aspect ratios. An explicit form of the parametric fit is provided which takes into account the hot- and cold-wall boundary layers in the liquid.

Nomenclature

$A_{0,1,2,3}$	$[-]$	coefficients for Re-dependent fits
Bi	$[-]$	Biot number and Biot function
Ca	$[-]$	capillary number
Ma	$[-]$	Marangoni number
Pr	$[-]$	Prandtl number
Re	$[-]$	Reynolds number
$\mathcal{V}$	$[-]$	volume ratio of the liquid bridge
$\boldsymbol{J}$	$[-]$	Jacobian matrix
$R,\ R_{\text{tc}},\ R_{\text{gap}}$	[m]	radius of rods, test chamber and annular gap around the liquid bridge
$T,\ \Delta T$	[K]	temperature and temperature difference
a	$[-]$	coefficients for z-dependent fits
d	[m]	distance between support rods
$\boldsymbol{f}$	$[-]$	residual of the Newton method
h_{fs}	$[-]$	free surface deformation
h_{g}	[W/(m^{2}K)]	heat-transfer coefficient (gas)
$p,\ \boldsymbol{u}$	$[-]$	pressure and velocity field
$r,\ \varphi,\ z$	$[-]$	radial, azimuthal, axial coordinate
$\boldsymbol{x}$	$[-]$	position vector
$\boldsymbol{y}$	$[-]$	solution of the Newton method
$\alpha,\ \beta$	$[-]$	coefficients for Γ-dependent fits
γ	[N/(mK)]	negative surface-tension coefficient
δ	$[-]$	increment of the Newton method
θ	$[-]$	reduced temperature
κ	[m^2/s]	thermal diffusivity
Λ	$[-]$	axial aspect ratio
λ	[W/(mK)]	thermal conductivity
ν	[m^2/s]	kinematic viscosity
ρ	[kg/m^3]	density
σ	[N/m]	surface tension
Γ	[m/s]	radial aspect ratio

Subscripts and Superscripts

0	evaluated at average temperature
$c1,\ c2$	boundary layer at the cold rod
DSD	dynamic surface deformation
m	polynomial fit in the middle of the liquid bridge
cold, hot	hot and cold support rods
fs	free surface
g	gas phase
l	liquid phase
k	k-th iteration of the Newton method
min, max	local minimum and local maximum of Bi
ref	reference (non-dimensional temperature)
h	boundary layer thickness on the hot rod
tc	test chamber
gap	annular gap between the liquid bridge surface and the test chamber wall

1 Introduction

When the interface between two immiscible fluids experiences a tangential temperature gradient, the resulting variable surface tension leads to thermocapillary forces, which can drive the flow in the two phases (1). A natural framework for thermocapillary flows are microfluidic systems, where surface forces become more important than volume forces and buoyancy does not overshadow Marangoni stresses. This is the case, e.g., for small droplets (2) or thin films (3), where the interfacial forces between two immiscible fluids play a key-role for the fluid flow. Thermocapillary convection is also important in industrial processes which involve large temperature gradients, e.g., welding (4), combustion (5) and crystal growth (6). For these reasons, much attention has been paid to thermocapillary flows in simplified configurations such as thermocapillary liquid films (7), cavities (8; 9; 10), annular pools (11) and liquid bridges (12).

Originally, the system of a liquid bridge has been proposed as a model for the floating-zone crystal-growth process (13). Later, it became a paradigm for thermocapillary flows. The multiphase flow is crucially determined by the heat transfer across the liquid–gas interface, because the driving force depends on the tangential temperature gradient. Despite of the importance of the heat transfer, for the sake of computational economy, the flow is typically modelled as a single-phase liquid flow, where an interfacial heat transfer is assumed in form of Newton's law of cooling with some ad hoc temperature distribution in the ambient gas (14; 15). The single-phase modeling limits the computational cost, and the parameter space reduces to the non-dimensional groups for the liquid flow and a few parameters characterizing the heat transfer to the ambient gas, often a constant Biot number only.

Even though the surrounding gas has a strong influence on the liquid flow and its stability (16; 17), most numerical simulations and linear stability analyses have assumed Newton's cooling law with constant Biot number (even zero, i.e. adiabatic conditions) or a fixed given heat flux (15). We shall show that both these assumptions are too simplistic to properly represent the heat transfer and the driving of the thermocapillary flow.

Starting from two-dimensional multiphase simulations, we aim at constructing a refined heat-transfer model in the form of Newton's cooling law. To take into account the thermal effect of the flow in the ambient gas the constant Biot number is replaced by a Biot function which depends on the axial coordinate along the free surface. A new, robust and physically motivated methodology is developed to derive this functional dependence. Moreover, the improved Biot function is given in explicit form which allows to readily supply a single-phase solver with an accurate thermal boundary condition.

In Sec. 2 the multiphase flow problem is defined mathematically; in Secs. 3 and 4 the numerical discretization and the methodology to derive the model are explained. Section 5 presents the improved heat-transfer model and some evidence for its robustness and accuracy is provided. Additional comments are given and conclusions are drawn in Sec. 6.

2 Problem Formulation

A droplet of an incompressible Newtonian liquid is suspended between two coaxial cylindrical rods of radius R, placed at a mutual distance d, forming a liquid bridge. The liquid has a density ρ and a temperature-dependent kinematic viscosity $\nu(T)$ and thermal diffusivity $\kappa(T)$. The rods are differentially heated at constant temperatures $T_{\text{cold}} = T_0 - \Delta T/2$ and $T_{\text{hot}} = T_0 + \Delta T/2$, respectively, where T_0 is the mean temperature and ΔT the temperature difference between the support rods. Due to the thermocapillary effect the temperature gradient along the free surface of the liquid bridge induces a thermocapillary shear-stress which drives the flow along the free-surface from the hot rod to the cold rod. Up to linear order, the temperature-dependent surface tension $\sigma(T)$ reads

$$\sigma(T) = \sigma_0 - \gamma(T - T_0), \tag{1}$$

where $\sigma_0 = \sigma(T_0)$ is the surface tension at the mean temperature T_0 and $\gamma = -\partial\sigma/\partial T|_{T=T_0}$ the negative surface-tension coefficient. Since $\gamma > 0$ is a positive constant for most liquid–gas combinations $\partial\sigma/\partial T < 0$ and the surface tension decreases linearly with the surface temperature.

The liquid bridge is surrounded by an annular chamber space filled with a Newtonian gas (assumed incompressible) with constant density ρ_{g}, kinematic viscosity ν_{g} and thermal diffusivity κ_{g}. The annular chamber has an outer radius $R_{\text{tc}} = R + R_{\text{gap}}$ and a height $d_{\text{tc}} = d_{\text{cold}} + d + d_{\text{hot}}$. The bounding walls are thermally insulating (see fig. 1). In the absence of gravity, thermocapillary stresses at the liquid–gas interface represent the only driving of the flow.

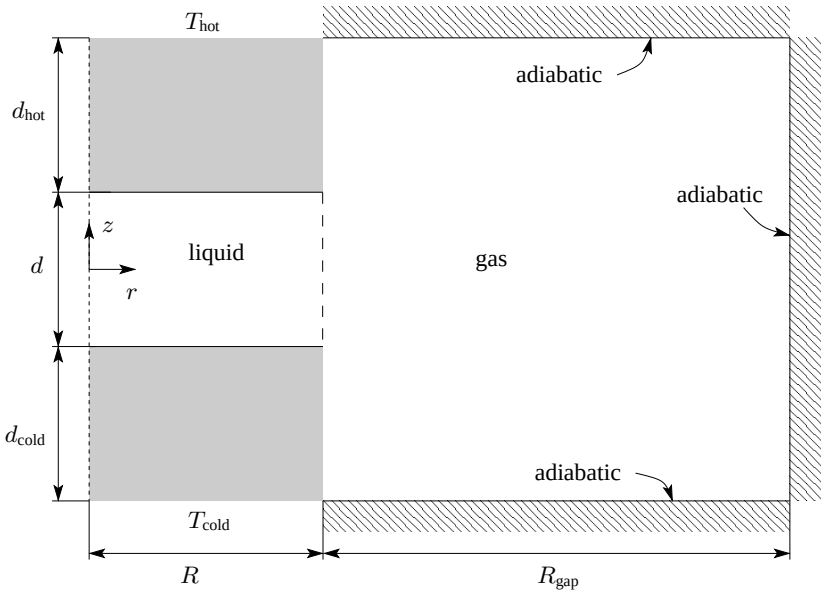

Figure 1: Sketch of the liquid bridge held in place by surface tension between the hot and the cold rod. The liquid bridge is surrounded by an ambient gas confined to an adiabatic test chamber.

Velocity, length, time, pressure and temperature are scaled with $\gamma\Delta T/\rho\nu_0$, d, $d\rho\nu_0/\gamma\Delta T$, $\gamma\Delta T d$ and ΔT, respectively (thermocapillary scaling). The resulting non-dimensional continuity, Navier–Stokes and energy equation for the steady flow are

$$\text{Re}\,(\boldsymbol{u}\cdot\nabla\boldsymbol{u}) = -\nabla p + \nabla\cdot(\nu/\nu_0\nabla\boldsymbol{u})\,, \tag{2a}$$

$$\nabla\cdot\boldsymbol{u} = 0, \tag{2b}$$

$$\text{Ma}\,(\boldsymbol{u}\cdot\nabla\theta) = \nabla\cdot(\kappa/\kappa_0\nabla\theta)\,, \tag{2c}$$

where $\nu_0 = \nu(T_0)$ and $\kappa_0 = \kappa(T_0)$ are the reference kinematic viscosity and thermal diffusivity, $\boldsymbol{x} = (r, \varphi, z)$ and t are polar space and time coordinates, $\boldsymbol{u} = (u, v, w)$ and p the velocity and pressure fields, and $\theta = (T - T_0)/\Delta T$ is the reduced temperature. Two non-dimensional groups arise, the thermocapillary Reynolds number Re and the Marangoni number Ma

$$\text{Re} = \frac{\gamma\Delta T d}{\rho\nu_0^2}, \quad \text{Ma} = \frac{\gamma\Delta T d}{\rho\nu_0\kappa_0}. \tag{3}$$

For comparison with other work, the Prandtl number $\text{Pr} = \text{Ma}/\text{Re} = \nu_0/\kappa_0$ is defined at the reference temperature. The geometry is characterized by the four aspect ratios (see fig. 1)

$$\Gamma = \frac{d}{R}, \quad \Gamma_{\text{tc}} = \frac{d}{R_{tc}}, \quad \Lambda_{\text{hot}} = \frac{d}{d_{\text{hot}}}, \quad \Lambda_{\text{cold}} = \frac{d}{d_{\text{cold}}}, \tag{4}$$

where, in the following, we fix the three aspect ratios $\Gamma_{\text{tc}} = d/R_{tc} = 0.1$ and $\Lambda_{\text{hot}} = \Lambda_{\text{cold}} = 1$ such that $\Lambda_{\text{tc}} = 1 + \Lambda_{\text{hot}} + \Lambda_{\text{cold}} = 3$, and vary $\Gamma = 0.5$, 0.66 and 1, which are values of common interest in the literature.

A major difficulty in solving (2) is the determination of the shape $h_{\text{fs}}(z)$ of the liquid–gas interface. Here we assume a pinning of the interface at the sharp circular edges of the rods, i.e. $h_{\text{fs}}(z = \pm 1/2) = 1/\Gamma$. Furthermore, we consider the limit of asymptotically large mean surface tension σ_0, for which the capillary number $\text{Ca} = \gamma \Delta T/\sigma_0 \to 0$. Using this approximation is justified for silicone oil liquid bridges: An asymptotic analysis of (18) has shown that the steady flow-induced interface deformations are typically smaller than 0.1% of the radius of the liquid bridge (see also (19)). Oscillatory flow-induced deformations were measured by (20) to be of the order of 0.1 microns. Thus, the dynamic oscillatory deformations were 10^5 times smaller than the length scale $h = 10\,\text{mm}$ of the liquid bridge (see also (21; 22)). Taking the limit $\text{Ca} \to 0$, flow-induced (liquid and gas) interfacial deformations are absent. Therefore, the interfacial shape is independent of the flow and can be determined by solving the Young–Laplace equation (12). In the absence of gravity and for unit non-dimensional volume of liquid

$$\mathcal{V} = \int_{-1/2}^{1/2} h_{\text{fs}}^2(z) \mathrm{d}z = 1, \tag{5}$$

the liquid bridge is cylindrical, i.e. $h_{\text{fs}} = 1/\Gamma$. The cylindrical shape of the liquid bridge is experimentally proven to be a good approximation for silicone oil liquid bridges.

The bulk equations (2) are solved assuming axisymmetry ($\partial_\varphi = 0$) and closed by the boundary conditions. Along the cold and hot support, no-slip and isothermal boundary conditions are enforced

$$\text{hot rod:} \quad \boldsymbol{u} = \boldsymbol{0}, \quad \theta = 1/2, \tag{6a}$$

$$\text{cold rod:} \quad \boldsymbol{u} = \boldsymbol{0}, \quad \theta = -1/2, \tag{6b}$$

whereas no-slip and adiabatic conditions are assumed at the walls of the test chamber

$$r = 1/\Gamma_{\text{tc}}: \quad \boldsymbol{u} = \boldsymbol{0}, \quad \partial_r \theta = 0, \tag{7a}$$

$$z = \pm \Lambda_{\text{tc}}/2: \quad \boldsymbol{u} = \boldsymbol{0}, \quad \partial_z \theta = 0. \tag{7b}$$

Finally, imposing kinematic boundary conditions, balancing the stresses and the heat fluxes and imposing continuity of velocity and temperature at the liquid–gas interface, respectively, yields

$$r = 1/\Gamma: \quad u = 0, \tag{8a}$$

$$(\nu_0/\nu)\partial_z \theta + \partial_r w = (\mu_{\text{g}}/\mu(T))\partial_r w_{\text{g}}, \tag{8b}$$

$$\partial_r \theta = (\kappa_{\text{g}}/\kappa(T))\partial_r \theta_{\text{g}} \tag{8c}$$

$$\boldsymbol{u} = \boldsymbol{u}_{\text{g}} \tag{8d}$$

$$\theta = \theta_{\text{g}}, \tag{8e}$$

where $\mu_{\text{g}} = \rho_{\text{g}} \nu_{\text{g}}$ and $\mu(T) = \rho \nu(T)$ are the dynamic viscosity of gas and liquid phase, respectively, w_{g} is the axial velocity in the surrounding gas and $\boldsymbol{u}_{\text{g}}$ and θ_{g} denote the velocity vector and the temperature in the gas phase, respectively.

3 Numerical Methods

The mathematical problem defined in Sec. 2 admits axisymmetric steady state solutions which are computed by means of the Newton–Raphson method

$$\boldsymbol{J}\left(\boldsymbol{y}^k\right) \cdot \delta \boldsymbol{y} = -\boldsymbol{f}\left(\boldsymbol{y}^k\right), \tag{9a}$$

$$\boldsymbol{y}^{k+1} = \boldsymbol{y}^k + \delta \boldsymbol{y}, \tag{9b}$$

where $\boldsymbol{J}\left(\boldsymbol{y}^k\right)$ is the Jacobian of (2), $\boldsymbol{y} = (u, w, p, \theta)^T$ the solution vector, k enumerates the iteration step, $\boldsymbol{f}\left(\boldsymbol{y}^k\right)$ is the nonlinear residual and $\delta \boldsymbol{y}$ the solution increment between the k-th and the $(k+1)$-th iteration.

Inserting (9b) in (2) and linearizing with respect to $\delta \boldsymbol{y}$ yields

$$\nabla \cdot \delta \boldsymbol{u} = -\nabla \cdot \boldsymbol{u}^k, \tag{10a}$$

$$\text{Re}\left(\delta \boldsymbol{u} \cdot \nabla \boldsymbol{u}^k + \boldsymbol{u}^k \cdot \nabla \delta \boldsymbol{u}\right) + \nabla \delta p - \nabla \cdot (\nu/\nu_0 \nabla \delta \boldsymbol{u}) = -\text{Re}\left(\boldsymbol{u}^k \cdot \nabla \boldsymbol{u}^k\right) - \nabla p^k + \nabla \cdot \left[\nu(T^k)/\nu_0 \nabla \boldsymbol{u}^k\right], \tag{10b}$$

$$\text{Ma}\left(\delta \boldsymbol{u} \cdot \nabla \theta^k + \boldsymbol{u}^k \cdot \nabla \delta \theta\right) - \nabla \cdot (\kappa/\kappa_0 \nabla \delta \theta) = -\text{Ma}\left(\boldsymbol{u}^k \cdot \nabla \theta^k\right) + \nabla \cdot \left[\kappa(T^k)/\kappa_0 \nabla \theta^k\right], \tag{10c}$$

where the convective term has been linearized by

$$\nabla \cdot \left(\boldsymbol{u}^{k+1}\boldsymbol{u}^{k+1}\right) \approx -\nabla \cdot \left(\boldsymbol{u}^{k}\boldsymbol{u}^{k}\right) + \nabla \cdot \left(\boldsymbol{u}^{k+1}\boldsymbol{u}^{k}\right) + \nabla \cdot \left(\boldsymbol{u}^{k}\boldsymbol{u}^{k+1}\right). \tag{11}$$

Equation (10) is solved using the same grid, initial guesses and convergence criteria as in (23).

4 Heat Transfer Model

The numerical solution of the steady multiphase Navier–Stokes system ensures a full thermal and mechanical coupling between the liquid and the gas phase. Hence, no additional models are required to determine the heat transfer between the liquid bridge and the surrounding gas. Post-processing the flow fields allows to compute the heat transfer across the interface. With θ and $\partial_r\theta|_l$ obtained from the numerical solution and evaluated at the free surface, the heat exchange at the liquid–gas interface can be recast in a Newton's cooling law

$$r = 1/\Gamma: \quad \mathrm{Bi} = \frac{\partial_r\theta|_l}{\theta - \theta_{\mathrm{ref}}}, \tag{12}$$

where the cold rod temperature $\theta_{\mathrm{ref}} = -1/2$ is used as the reference temperature. Equation (12) uses a non-standard definition of the Biot number, such that, if $\mathrm{Bi} > 0$, and $\theta > \theta_{\mathrm{ref}}$, then $\partial_r\theta|_l > 0$. Equation (12) can be understood as a definition of the local Biot number, or Biot function,

$$\mathrm{Bi}(z) = \frac{h_{\mathrm{g}}(z)d}{\lambda}, \tag{13}$$

where λ is the heat conductivity of the liquid and $h_{\mathrm{g}}(z)$ the heat-transfer coefficient of the gas. In this framework, the Biot function not only depends on z, but also on all other governing parameters, i.e. $\mathrm{Bi} = \mathrm{Bi}(z; \mathrm{Re}, \mathrm{Pr}, \Gamma, \mathrm{Pr_g}, \Gamma_{\mathrm{tc}}, ...)$.

The classical Newton's cooling law is based on a constant Biot number ($\mathrm{Bi} = 0$ for adiabatic free surface). This is a poor approximation to the actual heat transfer process. We aim at deriving a robust fit for $\mathrm{Bi}(z; \mathrm{Re}, \mathrm{Pr} = 28.5, \Gamma, \mathrm{Pr_g}, ...)$ assuming air as surrounding gas (i.e. $\mathrm{Pr_g} = 0.71$). Once the Biot function is known, (12) can be interpreted as a boundary condition for θ in the framework of a single-phase flow model. Using the Biot function, the single-phase model would yield almost the same flow and temperature field as the two-phase model, albeit with much less numerical effort.

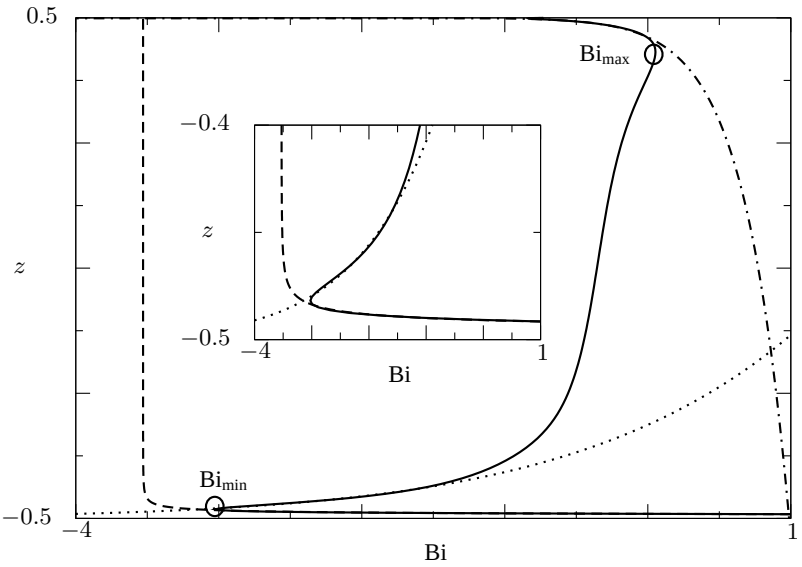

Figure 2: Biot function for $\mathrm{Pr} = 28.5$, $\Gamma = 0.5$, $\mathrm{Re} = 300$ and ambient air (full line). Power-law fits to $\mathrm{Bi}(z)$ in the region of the thermal boundary layers at the hot and cold wall are shown as dashed, dotted and dashed–dotted lines. The circles indicate the stationary points of $\mathrm{Bi}(z)$.

A typical Biot function is shown in fig. 2 (full line) for $\Gamma = 0.5$ and $\mathrm{Re} = 300$. Owing to the high Prandtl number, the temperature field in the liquid is subject to strong convective effects. The corresponding thermal boundary layers on the cold and the hot wall are reflected by the sharp minimum and maximum of the Biot function near the

edges $z = \pm 1/2$. The dependence of the Biot function in the boundary layer region is well captured by power laws (dashed, dotted and dashed–dotted lines in fig. 2). Moreover, the locations and the absolute values of the stationary points of $\mathrm{Bi}(z)$ (see fig. 2) are well described by the functional dependence

$$\{\delta_{\text{cold}}, \mathrm{Bi}_{\text{min}}, \delta_{\text{hot}}, \mathrm{Bi}_{\text{max}}\} \approx A_0 + A_1 \mathrm{Re} + A_2/\mathrm{Re}^{A_3}, \tag{14}$$

where $\delta_{\text{cold}} = z_{\text{min}}$ and $\delta_{\text{hot}} = 0.5 - z_{\text{max}}$ are the distances from the cold and hot wall of the minimum and maximum of the Biot function, respectively. $A_i = \alpha_i + \beta_i \Gamma$ are fit parameters which, to good approximation, depend linearly on Γ within the range $\Gamma \in [0.5, 1]$. This is demonstrated in fig. 3.

Based on the typical behavior shown in fig. 2, the dependence of $\mathrm{Bi}(z)$ in the layers at the hot and cold rods are represented by

$$z \in [z_{\text{max}}, 0.5] : \mathrm{Bi} \approx a_{0h} + a_{1h}(0.5 - z)^{a_{2h}} \tag{15a}$$

$$z \in \left[\frac{-0.5 + z_{\text{min}}}{2}, z_{\text{min}}\right] : \mathrm{Bi} \approx a_{0c1} + a_{1c1}(0.5 + z)^{a_{2c1}} \tag{15b}$$

$$z \in [z_{\text{min}}, z_{\text{min}} + 0.1] : \mathrm{Bi} \approx a_{0c2} + a_{1c2}(0.5 + z)^{a_{2c2}}. \tag{15c}$$

Adding these terms and including a polynomial of degree five to fit the intermediate behavior far away from the edges (middle part of the Biot function, subscript m) yields the functional form of the fit for the Biot function

$$\mathrm{Bi} = [a_{0h} + a_{1h}(0.5 - z)^{a_{2h}}] + \sum_{j=1}^{2} [a_{0cj} + a_{1cj}(z + 0.5)^{a_{2cj}}] + \sum_{i=0}^{5} a_{im} z^i, \tag{16}$$

where a_{ih}, a_{ic1} and a_{ic2} $(i = 0, 1, 2)$ and a_{im} $(i \in [0, ..., 5])$ are fit parameters. The constants can be collected $a_0 = a_{0h} + a_{0c1} + a_{0c2} + a_{0m}$, once the individual subregions have been fitted.

All coefficients are function of the aspect ratio Γ and the Reynolds number Re. By combining results from all simulations, the functional dependence of the fitting coefficients on Γ and Re will be obtained. The functional dependence (14) has been employed for fitting a_{ih}, a_{ic1} and a_{ic2}, and the result is reported in table 1. Such assumption is motivated by the ansatz for the fit of the stationary points of the Biot function. In order to achieve a robust fit, which can also elucidate the boundary layer scaling of $\mathrm{Bi}(z)$, we follow a multistage approach.

In a first step only the power laws (15) for the boundary layers are determined. Each fit requires the determination, by least squares, of three fit parameters. Since the fitting function is non-linear, a Newton method is employed to find the solution of the non-linear system resulting from the least squares minimization. Given an initial guess for the coefficients, the iteration is terminated when the absolute norm of the residuals of the fit coefficients is less than 10^{-8}. To obtain a robust fit, the fit protocol follows four stages.

I) all three coefficients are obtained by (15) fitting $\mathrm{Bi}(z)$ for each combination of $\Gamma \in \{0.5, 0.66, 1\}$ and $\mathrm{Re} \in [30, 1500]$;

II) the coefficient a_{0*} (where $* \in \{h, c1, c2\}$) is fitted by (14) and a successive fit operation is employed to find the coefficients α_i and β_i reported in table 1 (see fig. 4). Inserting the fit of a_{0*} in (15), the other two coefficients are obtained fitting $\mathrm{Bi}(z)$ for each combination of $\Gamma \in \{0.5, 0.66, 1\}$ and $\mathrm{Re} \in [30, 1500]$;

III) the coefficient a_{1*} is fitted by (14) and a successive fit operation is employed to find the coefficients α_i and β_i reported in table 1 (see fig. 5). The fit of a_{1*} is substituted in (15) together with the fit of a_{0*}. The last coefficient is computed fitting $\mathrm{Bi}(z)$ for each combination of $\Gamma \in \{0.5, 0.66, 1\}$ and $\mathrm{Re} \in [30, 1500]$;

IV) the coefficient a_{2*} is fitted by (14) and a successive fit operation is employed to find the coefficients α_i and β_i reported in table 1 (see fig. 6).

Once all the fit parameters of the power laws have been determined, (16) is employed to determine a_{im} in a single step using the same least squares and Newton–Raphson method employed for a_{*h}, a_{*c1} and a_{*c2}.

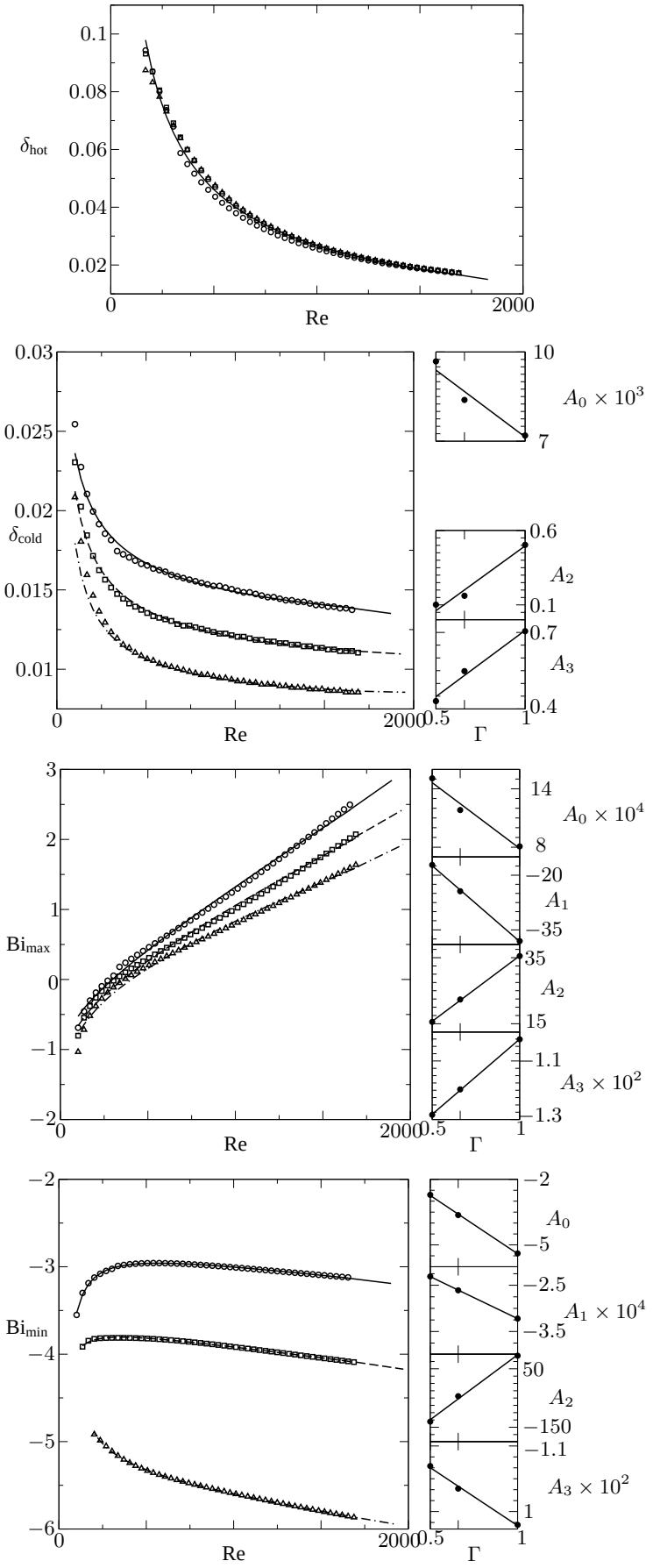

Figure 3: Minimum, Bi_{min}, and maximum, Bi_{max}, of the Biot function $\text{Bi}(z)$, and corresponding distance from the cold and hot rod, δ_{cold} and δ_{hot}, respectively. Markers refer to simulation data: $\Gamma = 0.5$ (circles, full line), 0.66 (squares, dashed line) and 1 (triangles, dash-dotted line). The lines refer to least square fits.

5 Results

The three successive fits corresponding to stages II, III, and IV, are demonstrated for $a_{0c2}(\Gamma, \mathrm{Re})$, $a_{1c2}(\Gamma, \mathrm{Re})$ and $a_{2c2}(\Gamma, \mathrm{Re})$ in figs. 4, 5 and 6, respectively. No continuation method is employed for educating the guess of a_{0*}, a_{1*} and a_{2*} depending on their value at a previous Reynolds number. This explains the scatter of a_{0*}, which is due to an underdetermination of the non-linear system to fit (see fig. 4). Reducing the underdetermination of the system by fixing a_{0*} leads to a much smaller scatter in stages III and IV for a_{1*} and a_{2*} (see figs. 5 and 6, respectively). As for the location and absolute value of the stationary points of the Biot function, also for a_{ih}, a_{ic1} and a_{ic2}, the fitting constants A_i are well approximated by a linear fit in Γ.

Table 1: Fit coefficients $A_i = \alpha_i + \beta_i \Gamma$, a_{ih}, a_{ic1} and a_{ic2} are fitted with the ansatz (14).

	a_{0h}	a_{1h}	a_{2h}
α_0	14.971	-14.089	0.00597
β_0	0	-11.215	-0.0124
α_1	-0.115	0.00353	-6.99×10^{-5}
β_1	0	-0.0016	2.86×10^{-5}
α_2	0	-2.277	0
β_2	0	9.190	0
α_3	0	-0.246	0
β_3	0	0.163	0
	a_{0c1}	a_{1c1}	a_{2c1}
α_0	-0.287	0	2.960
β_0	-6.254	0	-27.306
α_1	0	0	8.43×10^{-5}
β_1	0	0	-8.10×10^{-5}
α_2	0	0.743	2.787
β_2	0	0.491	26.183
α_3	0	0.587	0.0607
β_3	0	2.861	-0.0348
	a_{0c2}	a_{1c2}	a_{2c2}
α_0	-2.922	0.574	0.0301
β_0	-47.389	54.748	0.0149
α_1	0	-0.0014	2.70×10^{-6}
β_1	0	0.00410	9.25×10^{-6}
α_2	0	0	-14.204
β_2	0	0	46.087
α_3	0	0	1.079
β_3	0	0	0.599

In the next step all constant coefficients a_{0*} are gathered in a_0 and the remaining coefficients a_{im} for $i = 1, ..., 5$, are determined by inserting a_{1h}, a_{2h}, a_{1c1}, a_{2c1}, a_{1c2} and a_{2c2} into (16). The coefficient a_0 has been obtained by means of a free fitting operation shown in fig. 7. A successive fit of a_0 is done using the ansatz (14) with only $A_{0,1}$ and leads to $A_0 = 13.626 - 52.635\Gamma$ and $A_1 = -0.00297 - 0.00170\Gamma$.

In order to make the polynomial fit more robust, the other coefficients a_{im} have been found by means of a conditioned minimization of the least square distance as follows. Provided that the unconditioned fit for a_{im} (where $i = 1, ..., 5$) has been obtained for the lowest Reynolds number considered, $\mathrm{Re}_{\mathrm{min}} = 30$, the fit coefficients at higher Reynolds numbers are conditioned by $[a_{im}(\mathrm{Re}) - a_{im}(\mathrm{Re}_{\mathrm{min}}) - \mathrm{Re}/\mathrm{Re}_{\mathrm{min}} + 1] \in [-1, 1]$. The resulting fitting coefficients $a_{im}(\mathrm{Re}, \Gamma)$ can be downloaded from
`https://mega.nz/#!hQEmFIwY!9ybtrqWOqPd2NYYnafG0EpC5CeA3oJF5oB3DBUH1WKw` or
`http://www.ovgu.de/ifme/zeitschrift_tm/2019_Heft1/Fitting_Coefficients.zip`.

Employing the multi-stage methodology described in Sec. 4, a robust and physically motivated fit is obtained to model the Biot function for a wide range of thermocapillary Reynolds numbers and for all three aspect ratios of our study. A comparison between the Biot function obtained by the fit and the Biot function resulting from the multiphase numerical simulation shows a good agreement (fig. 8).

The importance of a robust heat-transfer model, which depends on the surrounding gas, is evident for numerical

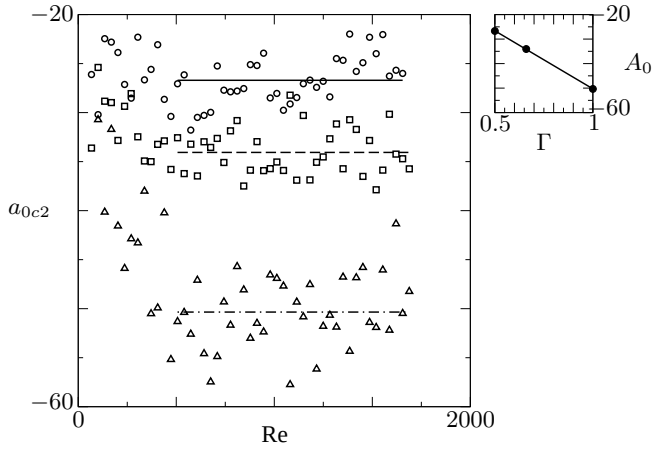

Figure 4: Fit of Bi(z) with respect to $a_{0c2}(\Gamma)$ (stage II, $z \in [z_{\min}, z_{\min} + 0.1]$) which is independent of Re (lines). Shown are data for $\Gamma = 0.5$ (circles, full line), 0.66 (squares, dashed line) and 1 (triangles, dash-dotted line). $A_0(\Gamma)$ is depicted as solid dots and the fit as a solid line in the side panel.

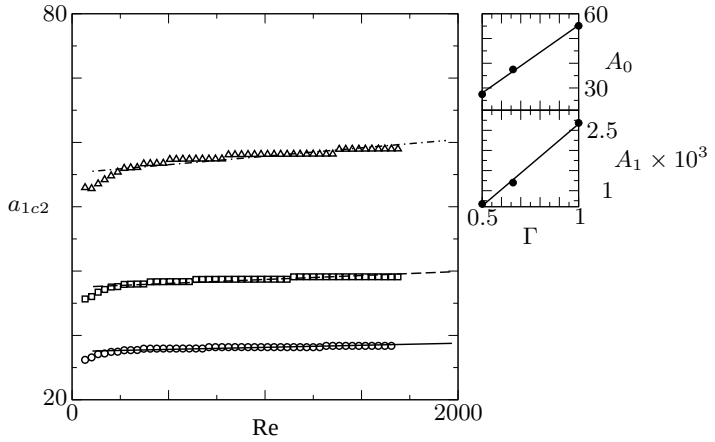

Figure 5: Fit of the coefficient a_{1c2} resulting after stage II. The open markers refer to the fit of the Biot number for $z \in [z_{\min}, z_{\min} + 0.1]$ and $\Gamma = 0.5$ (circles), 0.66 (squares) and 1 (triangles) after that a_{0c2} has been fixed as reported in table 1. The solid, dashed and dashed–dotted lines are the power-law fits employed to fit a_{1c2} for $\Gamma = 0.5$, 0.66 and 1, respectively. $A_{0,1}(\Gamma)$ are depicted as solid dots and the fits as a solid line in the side panels.

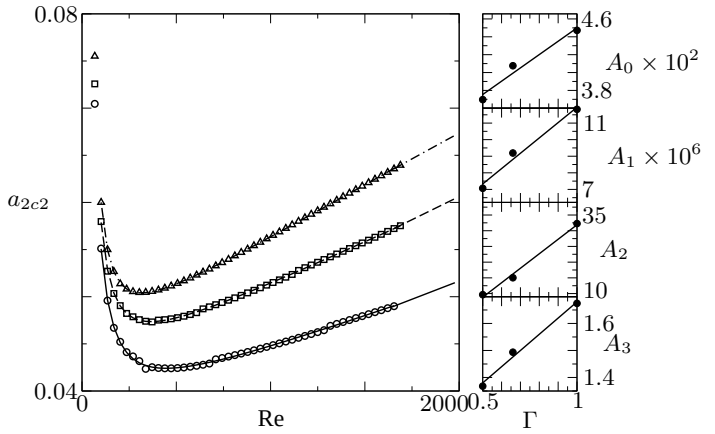

Figure 6: Fit of the coefficient a_{2c2} resulting after stage III. The open markers refer to the fit of the Biot number for $z \in [z_{\min}, z_{\min} + 0.1]$ and $\Gamma = 0.5$ (circles), 0.66 (squares) and 1 (triangles) after that a_{0c2} and a_{1c2} have been fixed as reported in table 1. The solid, dashed and dashed–dotted lines are the fits employed to fit a_{2c2} for $\Gamma = 0.5$, 0.66 and 1, respectively. $A_{0,1,2,3}(\Gamma)$ are depicted as solid dots and the fits as a solid line in the side panels.

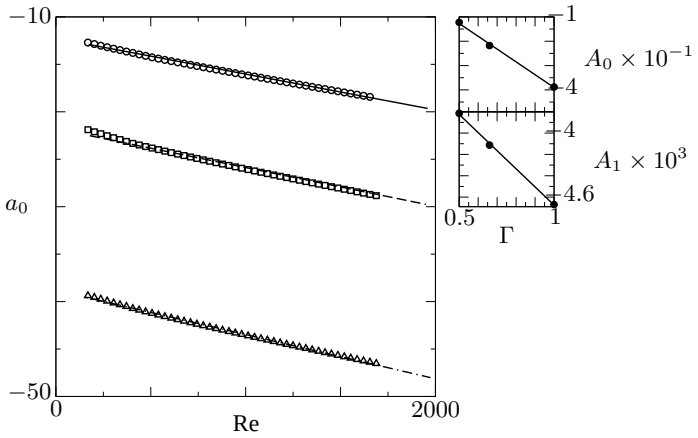

Figure 7: Fit of the coefficient $a_0 = a_{0h} + a_{0c1} + a_{0c2} + a_{0m}$. The open markers refer to the fit of the Biot number for $\Gamma = 0.5$ (circles), 0.66 (squares) and 1 (triangles) after that a_{1h}, a_{2h}, a_{1c1}, a_{2c1}, a_{1c2} and a_{2c2} have been fixed as reported in table 1. The solid, dashed and dashed–dotted lines are the fits employed for a_0 for $\Gamma = 0.5$, 0.66 and 1, respectively. $A_{0,1}(\Gamma)$ are depicted as solid dots and the fits as a solid line in the side panels.

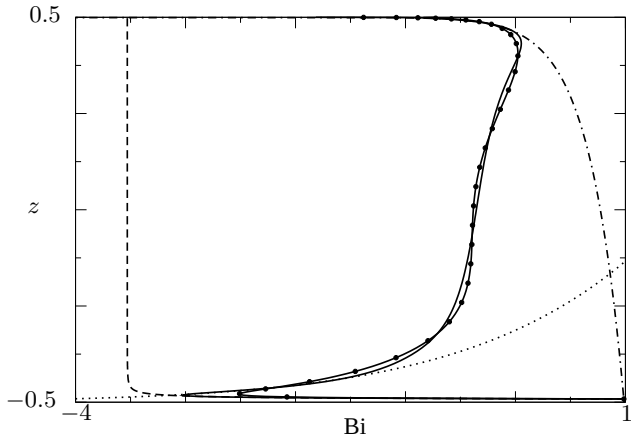

Figure 8: Comparison between the Biot function obtained from the multiphase simulation (solid line) and the corresponding fit obtained by the multi-stage approach of sec. 4 (solid line with full markers) for Pr $= 28.5$, Re $= 300$, $\Gamma = 0.5$. The dashed, dotted and dashed–dotted lines indicate the power laws fits within the three subranges.

simulations of the flow in thermocapillary liquid bridges and the onset of three-dimensional instabilities. The primary goal of the model is to replace (8c) by a boundary condition (12) which only involves the liquid phase and the Biot function. Since the viscous forces exerted by the gas on the interface can often be neglected ($\nu_g = 0$) this single-phase approach still leads to a reliable prediction of flow in the liquid bridge. The computational cost of a single-phase solver is much cheaper (saving about 70% for the present simulations cost) than the corresponding multiphase solver employed.

To demonstrate the effectiveness of using the Biot function in combination with a single-phase solver we compare the resulting free-surface velocity $|w_{fs}|$ employing different methods in fig. 9. The surface velocity obtained using the Biot function (dots) much better approximates the reference result of the two-phase simulation (full line) than the single phase solver using Bi $= 0$ (dashed line) or Bi $= -0.2$ (dashed–dotted line, value suggested by (24)). This clearly demonstrates the superiority of the Biot-function approach over the use of a constant unknown Biot number. The advantage is understood when inspecting a typical Biot function as in fig. 2: Only the region $z \in [-0.4, 0.4]$ may perhaps be approximated by a constant Biot number. The sharp variation of Bi(z) in the boundary layer region close to the hot and the cold walls, however, cannot be represented by Newton's heat-transfer law with a constant Biot number. The (false) modeling assumption of an adiabatic free surface leads to an increase and thinning of the velocity peak at the cold wall and too low surface velocities near the hot rod. A similar trend is observed for Bi $= -0.2$, even though the free-surface velocity compares slightly better with the multiphase simulation, in particular, near the cold corner (fig. 9).

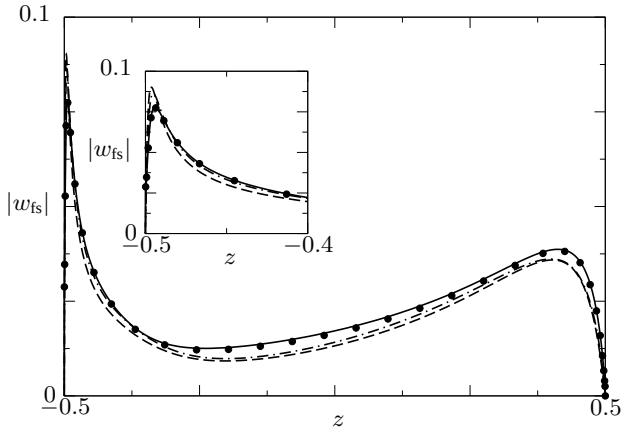

Figure 9: Comparison of the free surface velocity $|w_{\mathrm{fs}}|$ obtained by the multiphase solver (solid line), single-phase adiabatic solver (dashed line), single-phase solver with $\mathrm{Bi} = -0.2$ (dashed–dotted line) and single-phase solver supplied by our heat transfer model (full markers) for $\mathrm{Pr} = 28.5$, $\mathrm{Re} = 300$, $\Gamma = 0.5$.

6 Discussion and Conclusions

A correlation for the space-resolved heat transfer across the free surface between a liquid bridge and the ambient gas phase has been established. To that end fully-coupled, multiphase, axisymmetric simulations for a 2 cSt-silicone-oil liquid bridge surrounded by air have been carried out for a generic adiabatic air chamber. The heat transfer across the liquid–gas interface has been computed for 150 configurations varying the aspect ratio Γ of the liquid bridge and the thermocapillary Reynolds number Re, i.e. the strength of the flow.

Based on the two-phase data computed, a heat transfer model has been proposed in form of Newton's cooling law, but with a space-dependent Biot number which was called Biot function $\mathrm{Bi}(z)$. The Biot function, obtained by a multistage fit, well reproduces the characteristic strong variations of the heat transfer near the edges of the interface which are caused by the thermal boundary layers in the flow. The shape of the Biot function $\mathrm{Bi}(z)$ near the walls can be well represented by power laws. The resulting explicit fit compares very well with the heat transfer obtained from multiphase simulations without any a priori heat-transfer modeling.

Additional accurate calculations of the steady axisymmetric flow for $\mathcal{V} = 1$ have been carried out for $(\Gamma, \mathrm{Re}) \in \{0.5, 1\} \times \{30, 1500\}$, admitting dynamic, flow-induced surface deformations using the material properties of 2 cSt silicone oil. The calculations are based on the code `MaranStable` briefly described in section 4.2 of (17). In all four cases, the difference in the surface temperature when dynamic surface deformations are taken into account as compared to when they are neglected was nowhere larger than 3×10^{-3}. Moreover, computing the Biot function $\mathrm{Bi}_{\mathrm{DSD}}(z)$ taking into account the dynamic surface deformations (DSD) for the above cases, the difference $|\mathrm{Bi}_{\mathrm{DSD}}(z) - \mathrm{Bi}(z)|$ was always two orders of magnitude smaller than the confidence level of the fit used. These tests confirm that dynamic free surface deformations can be safely neglected for the parameters investigated.

The correlation derived in form of a Biot function can be supplied as a boundary condition to any single-phase solver. Corresponding single-phase simulations were shown to much better approximate the results of the fully coupled multiphase solver than any Newton law using a constant Biot number. Beyond the practical advantages of the present model to reduce the computational cost of multiphase solvers by equivalent single-phase solvers, we expect that the use of a Biot function will contribute to clarify the asymptotic scaling of $\mathrm{Bi}(z)$ in the boundary layer regions and help guiding experimental measurements of the heat transfer which are planned to be carried out under microgravity conditions (25).

Future work should aim at extending the parametric study presented, including the effect of gravity forces which are relevant for ground conditions, as the hydrostatic pressure does affect the shape of the liquid bridge. Furthermore, other liquids, gases and chamber geometries might be of interest.

Acknowledgements

We thank M. Stojanovic for calculating flows inclusive of dynamic surface deformations of the liquid–gas interface.

His contribution was made possible through FFG grant number 866027 under the Austrian Space Applications Programme ASAP14.

References

[1] Scriven, L.E., and Sternling, C.V., 1960, “The Marangoni effects”, *Nature*, Vol. 187, pp. 186–188.

[2] Young, N.O., Goldstein, J.S., and Block, M.J., 1959, “The motion of bubbles in a vertical temperature gradient”, *J. Fluid Mech.*, Vol. 6, pp. 350–356.

[3] Smith, M.K., and Davis, S.H., 1983, “Instabilities of dynamic thermocapillary liquid layers. Part 1. Convective instabilities”, *J. Fluid Mech.*, Vol. 132, pp. 119–144.

[4] Mills, K.C., Keene, B.J., Brooks, R.F., and Shirali, A., 1998, “Marangoni effects in welding”, *Philos. T. Roy. Soc. As*, pp. 911–926.

[5] Sirignano, W.A., and Glassman, I., 1970, “Flame spreading above liquid fuels: Surface-tension-driven flows”, *Combust. Sci. Technol.*, Vol. 1, pp. 307–312.

[6] Schwabe, D., 1981, “Marangoni effects in crystal growth melts”, *Physicochem. Hydrodyn.*, Vol. 2, pp. 263–280.

[7] Oron, A., Davis, S.H., and Bankoff, S.G., 1997, “Long-scale evolution of thin liquid films”, *Rev. Mod. Phys.*, Vol. 69, pp. 931–980.

[8] Carpenter, B.M., and Homsy, G.M., 1989, “Combined buoyant-thermocapillary flow in a cavity”, *J. Fluid Mech.*, Vol. 207, pp. 121–132.

[9] Xu, J., and Zebib, A., 1998, “Oscillatory two- and three-dimensional thermocapillary convection”, *J. Fluid Mech.*, Vol. 364, pp. 187–209.

[10] Kuhlmann, H.C., and Albensoeder, S., 2008. “Three-dimensional flow instabilities in a thermocapillary-driven cavity”, *Physical Review E*, Vol. 68, pp. 036303.

[11] Li, Y.-R., Peng, L., Akiyama Y., and Imaishi, N., 2003, “Three-dimensional numerical simulation of thermocapillary flow of moderate Prandtl number fluid in an annular pool”, *J. Cryst. Growth*, Vol. 259, pp. 374–387.

[12] Kuhlmann, H.C., 1999, “Thermocapillary Convection in Models of Crystal Growth”, *Springer*, Vol. 152.

[13] Hurle, D.T.J., and Jakeman, E., 1981, “Introduction to the techniques of crystal growth”, *Physicochem. Hydrodyn.*, Vol. 2, pp. 237–244.

[14] Nienhüser, C.H., and H. C. Kuhlmann, H.C., 2002, “Stability of thermocapillary flows in non-cylindrical liquid bridges”, *J. Fluid Mech.*, Vol. 458, pp. 35–73.

[15] Motegi, K., Kudo, M., and Ueno, I., 2017, “Linear stability of buoyant thermocapillary convection for a high-Prandtl number fluid in a laterally heated liquid bridge”, *Phys. Fluids*, Vol. 29, pp. 044106.

[16] Kamotani, Y., Wang, L., Hatta, S., Wang, A., and Yoda, S., 2003, “Free surface heat loss effect on oscillatory thermocapillary flow in liquid bridges of high Prandtl number fluids”, *Int. J. Heat Mass Transfer*, Vol. 46, pp. 3211–3220.

[17] Shevtsova, V., Gaponenko, Y., Kuhlmann, H.C., Lappa, M., Lukasser, M., Matsumoto, S., Mialdun, A., Montanero, J.M., Nishino, K., Ueno, I., 2014, “The JEREMI-project on thermocapillary convection in liquid bridges. Part B: overview on impact of co-axial gas flow”, *Fluid Dyn. Mater. Process.*, Vol. 10, pp. 197–240.

[18] Kuhlmann, H.C., Nienhüser, C., 2002, “Dynamic free-surface deformations in thermocapillary liquid bridges”, *Fluid Dyn. Res.*, Vol. 31, pp. 103–127.

[19] Shevtsova, V.M., Ermakov, M.K., Ryabitskii, E., Legros, J.C., 1997, “Oscillations of a liquid bridge free surface due to the thermal convection”, *Acta Astronaut.*, Vol. 41, pp. 471–479.

[20] Yano, T., Nishino, K., Matsumoto, S., Ueno, I., Komiya, A., Kamotani, Y., Imaishi, N., 2018. “Report on microgravity experiments of dynamic surface deformation effects on Marangoni instability in high-Prandtl-number liquid bridges”, *Microgravity Sci. Technol.*, Vol. 30, pp. 599–610.

[21] Ferrera, C., Mialdun, A., Shevtsova, V.M., Cabezas, M.G., Montanero, J.M., 2008, “Measurement of the dynamical free surface deformation in liquid bridges”, *Acta Astronaut.*, Vol. 62, pp. 471–477.

[22] Montanero, J.M., Ferrera, C., Shevtsova, V.M., 2008, “Experimental study of the free surface deformation due to thermal convection in liquid bridges”, *Exp. Fluids*, Vol. 45, pp. 1087–1101.

[23] Romanò, F., Kuhlmann, H.C., Ishimura, M., and Ueno, I., 2017, “Limit cycles for the motion of finite-size particles in axisymmetric thermocapillary flows in liquid bridges”, *Phys. Fluids*, Vol. 29, pp. 093303.

[24] Gaponenko, Y., and Shevtsova, V., 2012, “Heat transfer through the interface and flow regimes in liquid bridge subjected to co-axial gas flow”, *Microgravity Sci. Technol.*, Vol. 24, pp. 297–306.

[25] Nishino , K., Yano, T., Kawamura, H., Matsumoto, S., Ueno, I., and Ermakov, M.K., 2015, “Instability of thermocapillary convection in long liquid bridges of high Prandtl number fluids in microgravity”, *J. Cryst. Growth*, Vol. 420, pp. 57–63.

Address: [1]Dept. Biomed. Eng., University of Michigan, 2200 Bonisteel Blvd. Ann Arbor, MI 48109-2099, U.S.A.
Inst. Fluid Mech. Heat Transf., TU Wien, Getreidemarkt 9, 1060 Vienna, Austria.
e-mail: `frromano@umich.edu`

Address: [2]Institute of Fluid Mechanics and Heat Transfer, TU Wien, Getreidemarkt 9, 1060 Vienna, Austria.
e-mail: `hendrik.kuhlmann@tuwien.ac.at`